Numerical study of molten metal melt pool behaviour during conduction-mode laser spot melting

Ebrahimi, Amin; Kleijn, C.R.; Richardson, I.M.

DOI
10.1088/1361-6463/abca62

Publication date
2021

Document Version
Final published version

Published in
Journal of Physics D: Applied Physics

Citation (APA)
Ebrahimi, A., Kleijn, C. R., & Richardson, I. M. (2021). Numerical study of molten metal melt pool behaviour during conduction-mode laser spot melting. *Journal of Physics D: Applied Physics*, *54*(10), Article 105304. https://doi.org/10.1088/1361-6463/abca62

OPEN ACCESS
IOP Publishing
Journal of Physics D: Applied Physics
J. Phys. D: Appl. Phys. **54** (2021) 105304 (19pp)
https://doi.org/10.1088/1361-6463/abca62

Numerical study of molten metal melt pool behaviour during conduction-mode laser spot melting

Amin Ebrahimi[1], **Chris R Kleijn**[2] **and Ian M Richardson**[1]

[1] Department of Materials Science and Engineering, Delft University of Technology, Mekelweg 2, Delft 2628 CD, The Netherlands
[2] Department of Chemical Engineering, Delft University of Technology, van der Maasweg 9, Delft 2629 HZ, The Netherlands

E-mail: a.ebrahimi@tudelft.nl

Received 11 August 2020, revised 5 November 2020
Accepted for publication 13 November 2020
Published 22 December 2020

Abstract

Molten metal melt pools are characterised by highly non-linear responses, which are very sensitive to imposed boundary conditions. Temporal and spatial variations in the energy flux distribution are often neglected in numerical simulations of melt pool behaviour. Additionally, thermo-physical properties of materials are commonly changed to achieve agreement between predicted melt-pool shape and experimental post-solidification macrograph. Focusing on laser spot melting in conduction mode, we investigated the influence of dynamically adjusted energy flux distribution and changing thermo-physical material properties on melt pool oscillatory behaviour using both deformable and non-deformable assumptions for the gas-metal interface. Our results demonstrate that adjusting the absorbed energy flux affects the oscillatory fluid flow behaviour in the melt pool and consequently the predicted melt-pool shape and size. We also show that changing the thermo-physical material properties artificially or using a non-deformable surface assumption lead to significant differences in melt pool oscillatory behaviour compared to the cases in which these assumptions are not made.

Keywords: laser material processing, melt pool behaviour, thermocapillary flow, flow instabilities, free surface oscillation

(Some figures may appear in colour only in the online journal)

1. Introduction

Laser melting is being utilised for material processing such as additive manufacturing, joining, cutting and surface modification. The results of experimentation performed by Ayoola *et al* [1] revealed that the energy flux distribution over the melt-pool surface can affect melting, convection and energy transport in liquid melt pools and the subsequent re-solidification during laser melting processes. The imposed energy flux heats and melts the material and generates temperature gradients over the melt-pool surface. The resulting surface tension gradients and therefore Marangoni force is often the dominant force driving fluid flow, as can be understood virtually from the numerical investigation conducted by Oreper *et al* [2] and experimental observations reported by Mills *et al* [3]. Experimental investigations of Heiple *et al*[4] showed that the presence of surfactants in molten materials can alter Marangoni convection in the melt pool, and thus the melt-pool shape. Moreover, Paul *et al* [5] reported that the smoothness of the melt pool surface decreases when surfactants are present in the melt pool. However, according to the literature survey

conducted by Cook *et al* [6], the influence of surfactants on variations of surface tension and its temperature gradient is often neglected in numerical simulations of welding and additive manufacturing. DebRoy and David [7] stated that fluid flow in melt pools can lead to deformation and oscillation of the liquid free surface and can affect the stability of the process and the structure and properties of the solid materials after re-solidification. Aucott *et al* [8] confirmed that transport phenomena during fusion welding and additive manufacturing processes are characterised by highly non-linear responses that are very sensitive to material composition and imposed heat flux boundary conditions. Numerical models capable of predicting the melt pool behaviour with a sufficient level of accuracy are thus required to gain an insight into the physics of fluid flow and the nature of flow instabilities that are not accessible experimentally.

To avoid excessive simulation complexity and execution time in numerical simulations, the melt pool in such simulations is often decoupled from the heat source, the latter being incorporated as a boundary condition at the melt-pool surface. These boundary conditions should be imposed with a sufficient level of accuracy, as it is known from the work of Zacharia *et al* [9] that modelling the interfacial phenomena is critical to predicting the melt pool behaviour. Numerical studies on melt pool behaviour reported in the literature use both deformable and non-deformable surface assumptions for the gas-metal interface. Comparing the melt-pool shapes predicted using both deformable and non-deformable surface assumptions, Ha and Kim [10] concluded that free-surface oscillations can enhance convection in the melt pool and influence the melt-pool shape. Shah *et al* [11] reported that the difference between melt-pool shapes obtained from numerical simulations with deformable and non-deformable surface assumptions depends on the laser power. Three-dimensionality of the molten metal flow in melt pools, as observed experimentally by Zhao *et al* [12] and numerically by Kidess *et al* [13], is often neglected in numerical simulations. Moreover, when accounting for surface deformations, the volume-of-fluid (VOF) method developed by Hirt and Nichols [14], based on a Eulerian formulation, is the most common method for modelling the melt pool behaviour. In this diffuse boundary method, the interfacial forces and the energy fluxes applied on the melt-pool surface are treated as volumetric source terms in the surface region, instead of imposing them as boundary conditions. In this approach, however, the fact that surface deformations lead to temporal and spatial variations of the free surface boundary conditions, as remarked by Meng *et al* [15] and Wu *et al* [16], is often neglected. The results reported by Choo *et al* [17] suggest that variations in power-density distribution and changes in free-surface profile can affect molten metal flow in melt pools and its stability. Further investigations are essential to improve the understanding of the complex transport phenomena that happen during laser spot melting.

The aim of the present work is to analyse the effects of a dynamically adjusting energy flux distribution over the deforming liquid surface on the nature of fluid flow instabilities in partially-penetrated liquid melt pools. We will particularly focus on flow instabilities in low-Prandtl number liquid metal pools during conduction-mode laser spot melting; our results should however be relevant for a much wider range of materials processing technologies. Three-dimensional calculations are carried out to numerically predict the melt pool behaviour and thermocapillary-driven flow instabilities using various heat source implementation methods. Our study provides a quantitative representation and an understanding of the influence of heat flux boundary conditions on the transport phenomena and flow instabilities in the molten metal melt pool. Additionally, we discuss the influence of artificially enhanced transport coefficients on the melt-pool oscillatory behaviour.

2. Model description

2.1. Physical model

Laser spot melting of a metallic S705 alloy, as shown schematically in figure 1 and as experimentally studied by Pitscheneder *et al* [18], was numerically simulated as a representative example in the present work. A defocused laser-beam with a radius of $r_b = 1.4$ mm heats the bulk material from its top surface for 4 s. The laser-beam power Q is set to 3850 W with a top-hat intensity distribution. The averaged laser absorptivity of the material surface η is assumed to remain constant at 13% [18]. The absorbed laser power leads to an increase in temperature and subsequent melting of the base material. The base material is a rectangular cuboid shape with a base size ($L \times L$) of $24 \times 24\,\text{mm}^2$ and a height (H_m) of 10 mm, initially at an ambient temperature of $T_i = 300$ K. A layer of air with a thickness of $H_a =$ 2 mm is considered above the base material to monitor the gas-metal interface evolution. Except for the surface tension, the material properties are assumed to be constant and temperature independent and are presented in table 1. Although temperature-dependent properties can be employed in the present model to enhance the model accuracy, employing temperature-independent properties facilitates comparison of the results of the present work with previous results published in the literature [10, 19, 20], where temperature-independent material properties are employed. Moreover, further studies are required to enhance the accuracy of calculation and measurement of temperature-dependent material properties, particularly for the liquid phase above the melting temperature. The effects of employing temperature-dependent material properties on the thermal and fluid flow fields and melt-pool shape are discussed in detail in section 4.3. A change in surface-tension due to the non-uniform temperature distribution over the gas–liquid interface induces thermocapillary stresses that drive the melt flow. This fluid motion from low to high surface-tension regions changes the temperature distribution in the melt pool [21] and can lead to surface deformations that change the melt-pool shape and properties of the material after solidification [22]. The sulphur contained in the alloy can alter the surface tension of the molten material and its variations with temperature [23].

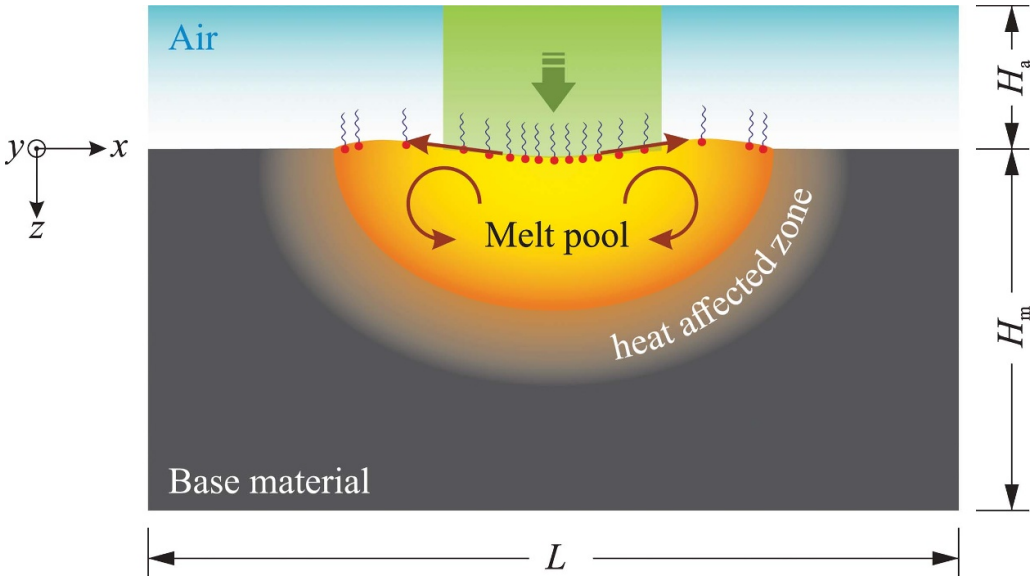

Figure 1. Schematic of conduction-mode laser spot melting.

Table 1. Thermophysical properties of the Fe-S alloy and air used in the present study. Values are taken from [20].

Property	Fe-S alloy	Air	Unit
Density ρ	8100	1.225	kg m^{-3}
Specific heat capacity c_p	670	1006	J kg^{-1} K^{-1}
Thermal conductivity k	22.9	0.024	W m^{-1} K
Viscosity μ	6×10^{-3}	1.8×10^{-05}	kg m^{-1} s^{-1}
Latent heat of fusion L_f	250800	–	J kg^{-1}
Liquidus temperature T_l	1620	–	K
Solidus temperature T_s	1610	–	K

2.2. Mathematical models

A three-dimensional multiphase model based on the finite-volume method was utilised to predict the melt pool dynamic behaviour and the associated transport phenomena. The present model is developed for conduction-mode laser melting. Further considerations will be required to develop the model for keyhole mode welding, including the complex laser-matter interactions, changes in surface chemistry and consequent surface tension variations for non- or partially shielded welding conditions. Both the molten metal and air were treated as Newtonian and incompressible fluids. Thermal buoyancy forces, which in laser spot melting are generally negligible compared to thermocapillary forces [24], were neglected both in the liquid metal and in the air. During conduction-mode laser-melting, the heat-source energy density is too low to cause significant vaporisation of the liquid metal [25], and the surface deformations are too small to cause multiple reflections of the laser rays at the liquid surface [26]. Furthermore, our preliminary results indicate that the maximum temperature of the melt pool is predominantly below 2700 K, significantly less than the boiling temperature of stainless steels, which is typically $\mathcal{O}(3100)$ K. Hence, multiple reflections and vaporisation were ignored. With this, the unsteady conservation equations of mass, momentum and energy were defined as follows:

$$\nabla \cdot \left(\rho \vec{V}\right) = 0, \tag{1}$$

$$\frac{\partial}{\partial t}\left(\rho \vec{V}\right) + \nabla \cdot \left(\rho \vec{V}\vec{V}\right) = -\nabla p + \nabla \cdot \left(\mu \nabla \vec{V}\right) + \vec{S}_d + \vec{F}_s, \tag{2}$$

$$\frac{\partial}{\partial t}(\rho h) + \nabla \cdot \left(\rho \vec{V} h\right) = \nabla \cdot \left(\frac{k}{c_p}\nabla h\right) - \frac{\partial}{\partial t}(\rho \Delta H) - \nabla \cdot \left(\rho \vec{V} \Delta H\right) + S_T, \tag{3}$$

where ρ is density, t time, $\vec{V}$ velocity vector, p pressure, μ dynamic viscosity, h sensible heat, k thermal conductivity, c_p specific heat capacity at constant pressure and ΔH latent heat. The enthalpy of the material H was defined as the sum of the latent heat and the sensible heat [27], and is expressed as

$$H = h + \Delta H = \left(h_{ref} + \int_{T_{ref}}^{T} c_p \, dT\right) + f_L L_f, \tag{4}$$

where h_{ref} is reference enthalpy, T_{ref} reference temperature, L_f latent heat of fusion, and f_L local liquid volume-fraction. Assuming the liquid volume-fraction in the metal to be a function of temperature only, a linear function [27] was used to calculate the liquid volume-fraction as follows:

$$f_L = \frac{T - T_s}{T_l - T_s}; \quad T_s \le T \le T_l, \tag{5}$$

where T_s and T_l are the solidus and liquidus temperatures, respectively.

To suppress fluid velocities in solid regions and to model fluid flow damping in the so-called "mushy zone", where phase transformation occurs within a temperature range

between T_s and T_l, a momentum sink term $\vec{S}_d$ [28] was implemented into the momentum equation as

$$\vec{S}_d = C\,\frac{(1-f_L)^2}{f_L^3+\epsilon}\,\vec{V}, \tag{6}$$

where C is the mushy-zone constant and ε is a small number to avoid division by zero as f_L approaches 0. The mushy-zone constant C was set to $10^7\,\mathrm{kg\,m^{-2}\,s^{-2}}$, which is large enough to dampen fluid velocities in solid regions according to the criterion defined by Ebrahimi *et al* [29], and ε was equal to 10^{-3}.

To capture the position of the gas–metal interface during melting, the volume-of-fluid (VOF) method developed by Hirt and Nichols [14] was utilised. This requires the solution of a transport equation for one additional scalar variable ϕ (*i.e.,* the so-called volume-of-fluid fraction) that varies between 0 in the gas phase and 1 in the metal phase:

$$\frac{\partial\phi}{\partial t} + \nabla\cdot\left(\phi\vec{V}\right) = 0. \tag{7}$$

Computational cells with $0 \le \phi \le 1$ are in the gas-metal interface region. The effective thermophysical properties of the fluid is then calculated using the mixture model as follows [30]:

$$\zeta = \phi\,\zeta_{\mathrm{metal}} + (1-\phi)\,\zeta_{\mathrm{gas}}, \tag{8}$$

where ζ corresponds to density ρ, viscosity μ, thermal conductivity k and specific heat capacity c_p.

Based on the method developed by Brackbill *et al* [31], surface tension and thermocapillary forces acting on the gas-metal interface were applied as volumetric forces in these interface cells and were introduced into the momentum equation as a source term $\vec{F}_s$ as follows:

$$\vec{F}_s = \vec{f}_s\|\nabla\phi\|\frac{2\rho}{\rho_{\mathrm{gas}}+\rho_{\mathrm{metal}}}, \tag{9}$$

where subscripts indicate the phase. The term $2\rho/(\rho_{\mathrm{gas}}+\rho_{\mathrm{metal}})$ was utilised to abate the effect of the large metal-to-gas density ratio by redistributing the volumetric surface-forces towards the metal phase (*i.e.,* the heavier phase). $\vec{f}_s$ is the surface force per unit area and was defined as follows:

$$\vec{f}_s = \sigma\kappa\vec{n} + \frac{\mathrm{d}\sigma}{\mathrm{d}T}\left[\nabla T - \vec{n}\,(\vec{n}\cdot\nabla T)\right], \tag{10}$$

where the first term on the right-hand side is the normal component, which depends on the value of surface tension and curvature of the melt-pool surface, and the second term is the tangential component that is affected by the surface tension gradient. In equation (10), σ is surface tension, and κ the surface curvature is

$$\kappa = -\left(\nabla\cdot\vec{n}\right), \tag{11}$$

and $\vec{n}$ the surface unit normal vector is

$$\vec{n} = \frac{\nabla\phi}{\|\nabla\phi\|}. \tag{12}$$

Table 2. The values used to calculate the surface tension of molten Fe–S alloy [23]

Property	Value	Unit
σ_m°	1.943	$\mathrm{N\,m^{-1}}$
$(\partial\sigma/\partial T)^\circ$	-4.3×10^{-4}	$\mathrm{N\,m^{-1}\,K^{-1}}$
Γ_s	1.3×10^{-5}	$\mathrm{mol\,m^{-2}}$
ψ	3.18×10^{-3}	–
a_s	150	–
ΔH°	-166.2×10^5	$\mathrm{J\,mol^{-1}}$

2.2.1. Surface tension. The temperature dependence of the surface tension of a liquid solution with a low concentration of surfactant can be approximated using a theoretical correlation derived on the basis of the combination of Gibbs and Langmuir adsorption isotherms as follows [32, 33]:

$$\sigma = \sigma^\circ - RT\Gamma_s\ln(1+Ka_s), \tag{13}$$

where σ is the surface tension of the solution, σ° the pure solvent surface tension, R the gas constant, Γ_s the adsorption at saturation, K the adsorption coefficient, and a_s the activity of the solute. From this, Sahoo *et al* [23] derived a correlation for binary molten metal–surfactant systems, including binary Fe–S systems:

$$\sigma = \sigma_m^\circ + \left(\frac{\partial\sigma}{\partial T}\right)^\circ(T-T_m) - RT\Gamma_s\ln\left[1+\psi a_s\exp\left(\frac{-\Delta H^\circ}{RT}\right)\right], \tag{14}$$

where σ_m° is the surface tension of pure molten-metal at the melting temperature T_m, ψ an entropy factor, ΔH° the standard heat of adsorption, and $(\partial\sigma/\partial T)^\circ$ the temperature coefficient of the surface tension of the pure molten-metal. Values of the properties used in equation (14) to calculate the temperature dependence of the surface tension of the molten Fe–S alloy are presented in table 2. Variations of the surface tension and its temperature coefficient are shown in figure 2 for an Fe–S alloy with 150 ppm sulphur content.

2.2.2. Laser heat source. The laser supplies a certain amount of energy (ηQ) to the material. Its energy input was modelled by adding a volumetric source term S_T to the energy equation (equation (3)) in cells at the gas–metal interface. The surface deformations affect the total energy input to the material [34]. This effect is generally not considered in numerical simulations of melt pool behaviour. To investigate the influence of surface deformations, five different methods for the heat-source implementation were considered.

2.2.2.1. Case 1, heat-source implementation without taking the influence of surface deformations on total energy input into consideration. In this case, the heat source model is defined as

$$S_T = \begin{cases} \frac{\eta Q}{\pi r_b^2}\|\nabla\phi\|\frac{2\rho c_p}{(\rho c_p)_{\mathrm{gas}}+(\rho c_p)_{\mathrm{metal}}}, & \text{if } r \le r_b \\ 0, & \text{otherwise} \end{cases} \tag{15}$$

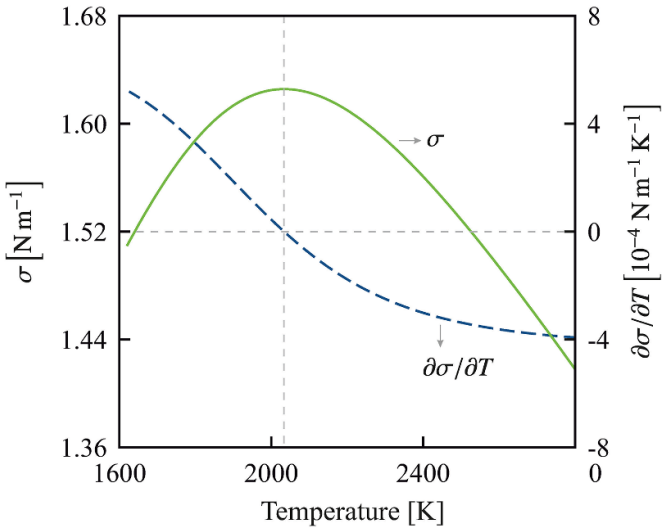

Figure 2. Variations of surface tension (green solid-line) and its temperature gradient (blue dashed-line) as a function of temperature obtained from equation (14) for an Fe–S alloy containing 150 ppm sulphur.

where r is radius defined as $\sqrt{x^2+y^2}$. This method is the most common method in modelling melt-pool surface oscillations without having a deep penetration (keyhole formation) (see for instance, [25, 26]). However, variations in the total energy input caused by a change in melt-pool surface shape, through changes in $\|\nabla\phi\|$, causing $\iiint_{\forall} S_T \,\mathrm{d}V$ to be different from ηQ, are an inherent consequence of using this method. Additionally, every segment of the melt-pool surface is exposed to the same amount of energy input regardless of the local surface orientation.

2.2.2.2. Case 2, heat source adjustment. To conserve the total energy input, an adjustment coefficient ξ was introduced to the heat source model as follows:

$$S_T = \begin{cases} \frac{\xi\eta Q}{\pi r_b^2}\|\nabla\phi\|\frac{2\rho c_p}{(\rho c_p)_{gas}+(\rho c_p)_{metal}}, & \text{if } r \le r_b \\ 0, & \text{otherwise} \end{cases} \tag{16}$$

where ξ was evaluated at the beginning of every time-step and was defined as

$$\xi = \frac{\eta Q}{\iiint_{\forall} S_T \,\mathrm{d}V}, \tag{17}$$

where $\forall$ stands for the computational domain. Utilising this technique for welding simulations has already been reported in the literature (see for instance, [15, 16, 34, 35]). Variations in energy absorption with deformations of the melt-pool surface are, however, not taken into consideration in this method.

2.2.2.3. Case 3, heat source redistribution. In this case, the energy flux was redistributed over the melt-pool surface assuming the energy absorption is a function of the local surface orientation. Accordingly, the local energy absorption is a maximum where the surface is perpendicular to the laser ray and is a minimum where the surface is aligned with the laser ray [36, 37]. This represents a simplified absorptivity model based on the Fresnel's equation [38] and is expressed mathematically, assuming the laser rays being parallel and in the z-direction, as follows:

$$S_T = \begin{cases} \frac{\eta Q}{\pi r_b^2}\|\nabla\phi\|\frac{2\rho c_p}{(\rho c_p)_{gas}+(\rho c_p)_{metal}}\left|\frac{\nabla\phi[z]}{\|\nabla\phi\|}\right|. & \text{if } r \le r_b \\ 0. & \text{otherwise} \end{cases} \tag{18}$$

the total energy input is not necessarily conserved in this method.

2.2.2.4. Case 4, heat source redistribution and adjustment. Utilising the same technique introduced in Case 2, the heat source model in Case 3 was adjusted to guarantee that total energy input is conserved. Hence, the heat source model was defined as

$$S_T = \begin{cases} \frac{\xi\eta Q}{\pi r_b^2}\|\nabla\phi\|\frac{2\rho c_p}{(\rho c_p)_{gas}+(\rho c_p)_{metal}}\left|\frac{\nabla\phi[z]}{\|\nabla\phi\|}\right|. & \text{if } r \le r_b \\ 0. & \text{otherwise} \end{cases} \tag{19}$$

2.2.2.5. Case 5, Flat non-deformable free surface. In this case, the surface was assumed to remain flat. Thermocapillary shear stresses caused by a non-uniform temperature distribution on the gas-metal interface were applied as a boundary condition, hence modelling the gas phase was not required. Consequently, the total energy absorbed by the surface was fixed in this method. The boundary conditions are described in section 2.2.3.

Table 3 presents a summary of the cases considered in the present work.

2.2.3. Boundary conditions. The bottom and lateral surfaces of the metal part were modelled to be no slip walls, but in fact they remain solid during the simulation time. At the boundaries of the gas layer above the metal part, a constant atmospheric pressure was applied (*i.e.*, $p = 101.325$ kPa) allowing air to flow in and out of the domain. The outer boundaries of the computational domain were modelled as adiabatic since heat losses through these boundaries are negligible compared to the laser power [20].

For Case 5, in which no gas layer is modelled explicitly, a thermocapillary shear-stress was applied as a boundary condition in the molten regions of the top surface. In the irradiated region on the material top-surface, a constant uniform heat flux was applied, while outside of this region the surface was assumed to be adiabatic [18]. The thermal and thermocapillary shear-stress boundary conditions were defined, respectively, as

$$k\frac{\partial T}{\partial \vec{n}} = \begin{cases} \frac{\eta Q}{\pi r_b^2}, & \text{if } r \le r_b \\ 0, & \text{otherwise} \end{cases} \tag{20}$$

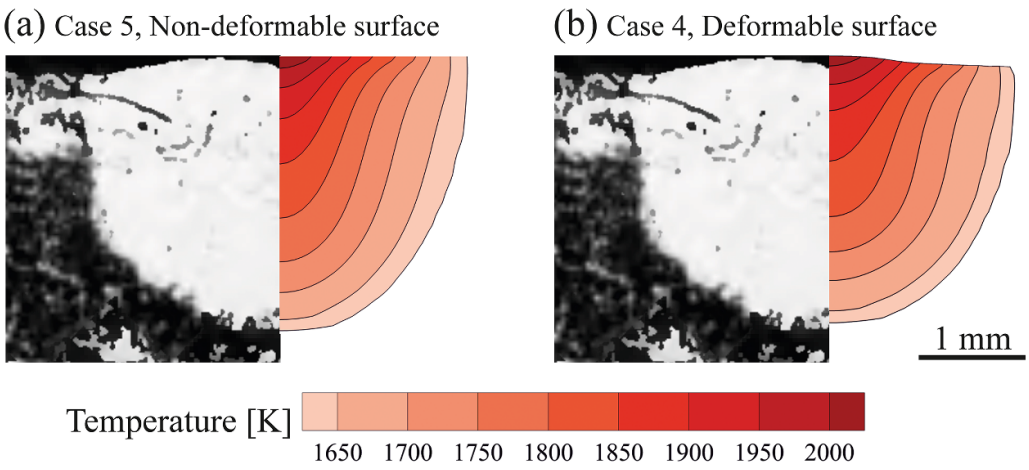

Figure 3. Comparison of the numerically predicted melt-pool shape after 5 s of heating with the corresponding experimentally measured post-solidification melt-pool shape reported by Pitscheneder *et al* [18]. Laser power was set to 3850 W and the material contains 150 ppm sulphur. Numerical predictions obtained from the present model assuming (a) non-deformable (Case 5) and (b) deformable gas-metal interface (Case 4).

and

$$-\mu\frac{\partial\vec{V}_{\mathrm{t}}}{\partial\vec{n}}=\frac{\mathrm{d}\sigma}{\mathrm{d}T}\frac{\partial T}{\partial\vec{\tau}}, \tag{21}$$

where $\vec{V}_{\mathrm{t}}$ is the tangential velocity vector, and $\vec{\tau}$ the tangential vector to the top surface.

3. Numerical procedure

The model was developed within the framework of the proprietary computational fluid dynamics solver ANSYS Fluent [39]. The laser heat source models and the thermocapillary boundary conditions as well as the surface-tension model were implemented through user-defined functions. After performing a grid independence study (results are presented in appendix A), a grid containing 8.6×10^{5} non-uniform hexahedral cells was utilised to discretise the computational domain. Minimum cell spacing was 2×10^{-5} m close to the gas-metal interface and 3×10^{-5} m in the melt pool central region. Cell sizes gradually increase towards the domain outer boundaries. The computational domain employed in the numerical simulations is shown in appendix A. The diffusion and convection terms in the governing equations were discretised using the central-differencing scheme with second order accuracy. For the pressure interpolation, the "pressure staggering option" (PRESTO) scheme [40] was used. Pressure and velocity fields were coupled employing the "pressure-implicit with splitting of operators" (PISO) scheme [41]. An explicit compressive VOF formulation was utilised for the spatial discretisation of the gas-metal interface advection [42]. The transient advection terms were discretised using a first order implicit scheme. To obtain a Courant number ($\mathrm{Co}=\|\vec{V}\|\Delta t/\Delta x$) less than 0.25, with velocity magnitudes up to $\mathcal{O}(1)\,\mathrm{m\,s^{-1}}$, the time-step size was set to 10^{-5} s. Each simulation was executed in parallel on 40 cores (Intel Xeon E5-2630 v4) of a high-performance computing cluster. Scaled residuals of the energy, momentum and continuity equations of less than 10^{-10}, 10^{-8} and 10^{-7} respectively, were defined as convergence criteria.

Table 3. Summary of the cases studied in the present work and the features included in the model for each case.

Name	Deformable free-surface	Heat source adjustment	Heat source redistribution
Case 1	Yes	No	No
Case 2	Yes	Yes	No
Case 3	Yes	No	Yes
Case 4	Yes	Yes	Yes
Case 5	No	No	No

4. Results and discussion

4.1. Model validation and solver verification

To verify the reliability and accuracy of the present numerical simulations, the melt-pool shapes obtained from the present simulations, for the problem introduced in section 2.1, are compared to experimental observations reported by Pitscheneder *et al* [18]. Figure 3 shows a comparison between the melt-pool shape obtained from the numerical simulation after 5 s of heating and the post-solidification experimental observation, which indicates a reasonable agreement. The maximum absolute deviations between the present numerical predictions and experimental data for the melt-pool width and depth is less than 5% and 2%, respectively. However, it should be noted that the thermal conductivity and viscosity of the liquid material were artificially increased in the simulations by a factor $\mathcal{F}=7$ with respect to their reported experimental values, as suggested by Pitscheneder *et al* [18]. This is known as employing an 'enhancement factor', mainly to achieve agreement between numerical and experimental results [19]. Independent studies conducted by Saldi *et al* [19] and Ehlen *et al* [43] revealed that without using

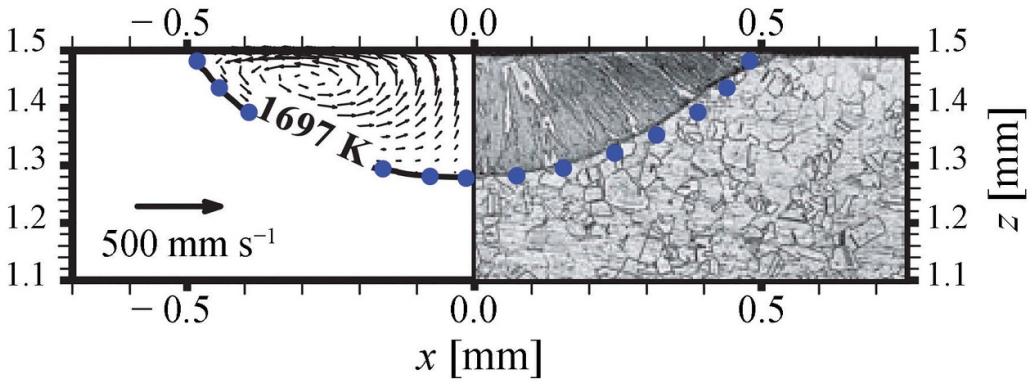

Figure 4. Comparison of the spot melt-pool shape obtained from the present numerical simulation with the corresponding experimentally observed (the right side of the figure) and numerically predicted (the left side of the figure) post-solidification melt-pool shape reported by He *et al* [49]. Laser power was set to 1967 W and the beam radius was 570 μm. Blue circles show the melt-pool shape predicted using the present model. The 500 mm s^{-1} reference vector is provided for scaling the velocity field shown in the melt pool.

such an enhancement factor, the fluid flow structure and the melt-pool shape in simulations differ drastically from experimental observations. The use of an enhancement factor is often justified by the possible occurrence of turbulence and its influence on heat and momentum transfer in the melt pool, which is assumed to be uniform in the melt pool. However, the high-fidelity numerical simulations conducted by Kidess *et al* [13, 20] on a melt pool with a flat non-deformable melt-pool surface revealed that turbulent enhancement is strongly non-uniform in the melt pool, resulting in an ω-shaped melt pool that differs notably from the results of simulations assuming uniform transport enhancement. We extended this study and performed a high-fidelity simulation based on the large eddy simulation (LES) turbulence model and took the effects of surface deformations into consideration [44] and showed that for the conduction-mode laser melting problem we considered, the influence of surface oscillations on melt pool behaviour is larger compared to the effects of turbulent flow in the melt pool; nevertheless the results do not agree with experiments without using some enhancement. These observations along with previous studies [19, 43, 45] suggest that the published weld pool models lack the inclusion of significant physics. The neglect in simulations of relevant physics such as chemical reactions and unsteady oxygen absorption by the melt-pool surface, non-uniform unsteady surfactant distribution over the melt-pool surface, re-solidification, free surface evolution and three-dimensionality of the fluid flow field has been postulated as reasons why such an *ad hoc* and unphysical enhancement factor is needed to obtain agreement with experimental data [46–48]. However, the inclusion of such factors will increase the model complexity and computational costs. Further investigations are essential to realising the problem with sufficient details. In section 4.4, the effects of the value used for the enhancement factor $\mathcal{F}$ on the thermal and fluid flow fields and melt-pool oscillatory behaviour are discussed in more detail.

The experimental and numerical data reported by He *et al* [49], who investigated unsteady heat and fluid flow in the melt pool during conduction-mode laser spot welding of stainless steel (AISI304) plates, were considered to validate the reliability of the present model. The melt pool shape obtained from the present model assuming a non-deformable free surface (Case 5) was compared with experimental and numerical data reported by He *et al* [49] and the results are shown in figure 4. In this problem, the laser power was set to 1967 W, the beam radius was 570 μm and laser pulse duration was 3 ms. The thermal conductivity and viscosity of the molten material were artificially increased in the simulations by a factor $\mathcal{F} = 17$ and $\mathcal{F} = 11$, respectively, as suggested by He *et al* [49]. The maximum absolute deviations between the present numerical predictions and experimental data for the melt-pool width and depth is less than 8% and 2.5%, respectively. The results obtained from the present model are indeed in reasonable agreement with the reference data, indicating the validity of the present model in reproducing the results reported in literature.

The reliability of the present model was also investigated by comparing the numerically predicted melt-pool size and surface deformations with experimental observations of Cunningham *et al* [50]. The evolutions of the melt-pool shape and its surface depression under stationary laser melting of a Ti-6Al-4V plate under conduction mode were studied. In this problem, the laser power is 156 W and has a Gaussian distribution and the radius of the laser spot is 7×10^{-5} m. The thermophysical properties of Ti-6Al-4V suggested by Sharma *et al* [51] were employed for calculations. Since the melt pool surface temperature reaches the boiling point, the effects of recoil pressure p_r and evaporation heat loss q_e were included in the model. The recoil pressure [52] and evaporation heat loss [53] were determined respectively as follows:

$$p_r = 0.54 \cdot P_0 \exp\left(\frac{L_v M\,(T - T_v)}{RTT_v}\right), \tag{22}$$

$$q_e = -0.82\frac{L_v M}{\sqrt{2\pi MRT}} P_0 \exp\left(\frac{L_v M\,(T - T_v)}{RTT_v}\right), \tag{23}$$

where P_0 is the ambient pressure, L_v the latent heat of vaporisation, M the molar mass, R the universal gas constant, T

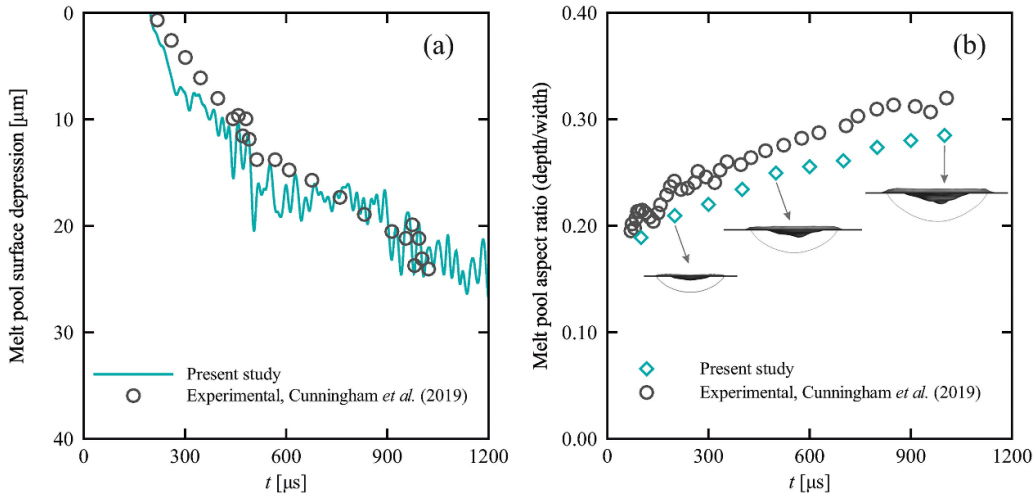

Figure 5. Comparison of (a) the melt-pool surface depression and (b) the melt pool aspect ratio (depth to width ratio) obtained from the present numerical simulation with the corresponding experimental observations of Cunningham *et al* [50]. Laser power was set to 156 W and the beam radius was 70 μm. Snapshots of the melt pool and its deformed surface are shown in the right subfigure for three different time instances.

the temperature and $T_v = 3315$ K the evaporation temperature. The results obtained from the present numerical simulations using the heat source model introduced for Case 4 are compared with those reported by Cunningham *et al* [50] in figure 5, which show a reasonable agreement. The maximum absolute deviations between the present numerical predictions and experimental data for the melt-pool aspect ratio is less than 12%.

Particular attention was also paid to the effect of spurious currents on numerical predictions of molten metal flow in melt pools with free surface deformations. Spurious currents are an unavoidable numerical artefact generating unphysical parasitic velocity fields that do not vanish with grid refinement when using the continuum surface force technique for modelling surface tension effects in the VOF method. This problem has been thoroughly investigated by Mukherjee *et al* [54] and the results of their study show that the Reynolds number based on the time-averaged maximum spurious velocity is $\mathcal{O}(10)$. The results of the present simulations show that the flow Reynolds number is $\mathcal{O}(10^3)$ that is at least two orders of magnitude larger than that induced by spurious currents. Furthermore, to suppress fluid velocities in the solid regions a momentum sink term is defined based on the enthalpy porosity technique that further weakens the spurious currents in solid regions. Therefore, the influence of spurious currents on numerical predictions is considered to be negligible in the present study.

4.2. The influence of heat source adjustment

When accounting for surface deformations, the volume-of-fluid (VOF) method developed by Hirt and Nichols [14], based on a Eulerian formulation, is the most common method for modelling the melt pool behaviour. In this diffuse boundary method, the interfacial forces and the energy fluxes applied on the melt-pool surface are treated as volumetric source terms in the surface region, instead of imposing them as boundary conditions. In this approach, however, the fact that surface deformations lead to temporal and spatial variations of the free surface boundary conditions, as remarked by Meng *et al* [15] and Wu *et al* [16], is often neglected. The results reported by Choo *et al* [17] suggest that variations in power-density distribution and changes in free-surface profile can affect molten metal flow in melt pools and its stability. In this section, the influence of applying each of the five different approaches to model the laser heat source (described as Cases 1–5 in section 2.2.2) on the melt pool behaviour is discussed. In these simulations, no enhancement factor, as introduced in the previous section, was employed since it is *ad hoc* and has little justification in physical reality.

The energy flux distribution over the melt-pool surface determines the spatial temperature distribution over the melt-pool surface and its temporal variations. Due to the temporal changes in the melt-pool surface shape, the total energy absorbed by the material in Case 1 varies between 491.4 W and 538.1 W, with a median value of 515.7 W, which differs from the total energy supplied by the laser $\eta Q = 500.5$ W. This issue is resolved by utilising a dynamic adjustment coefficient in Case 2, while the relative energy flux distribution remains unchanged. However, the results reported by Courtois *et al* [55] and Bergström *et al* [56] showed that the energy flux distribution varies with surface deformation during a laser melting process. When surface deformations are too small to cause multiple reflections, redistributing the energy flux over the free surface results in a better input energy conservation as obtained in Case 3. The total energy absorbed by the material in Case 3 ranges between 482.6 W and 532.3 W, with a median value of 503.8 W. By further introducing an adjustment coefficient (equation (17)), the absorbed energy can be made to exactly match the supplied laser power ηQ. Finally, for the most simple approach without any surface deformations (*i.e.,* Case 5), the total absorbed energy exactly matches the supplied laser power and remains unchanged in time.

The variations of temperature distribution over the melt-pool surface over time determine the thermocapillary driven

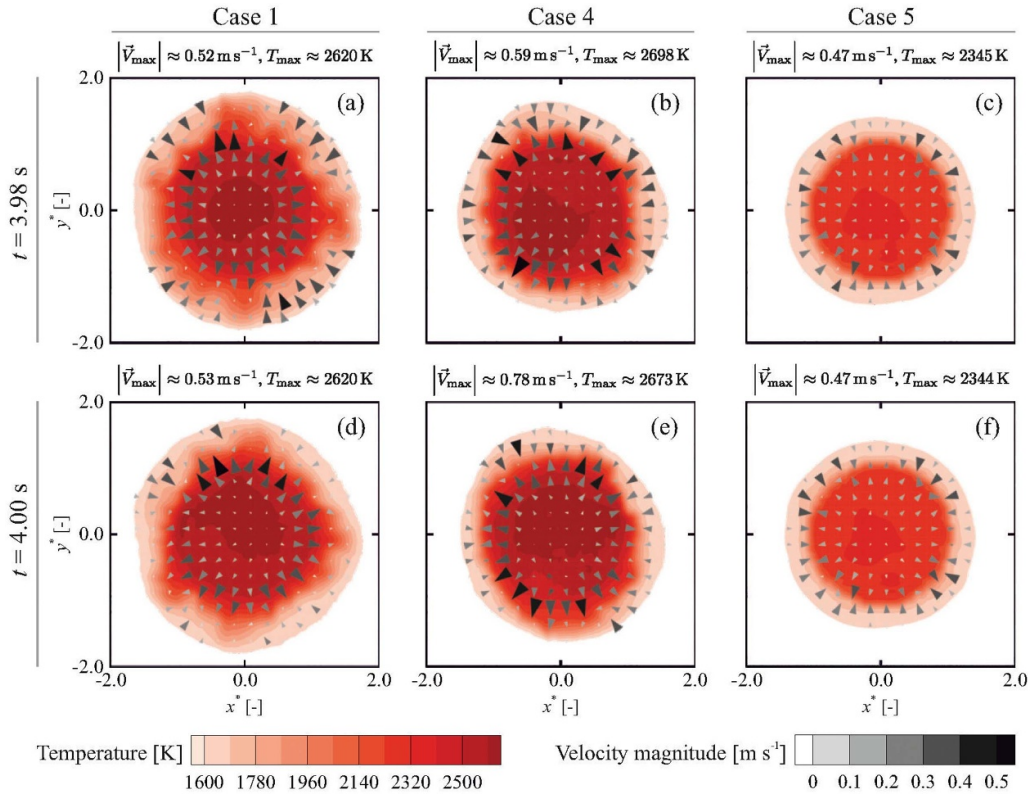

Figure 6. Contours of temperature and the velocity vectors on the melt pool free surface at two different time instances for Cases 1, 4 and 5. Coordinates are non-dimensionalised using the laser-beam radius r_b as the characteristic length scale.

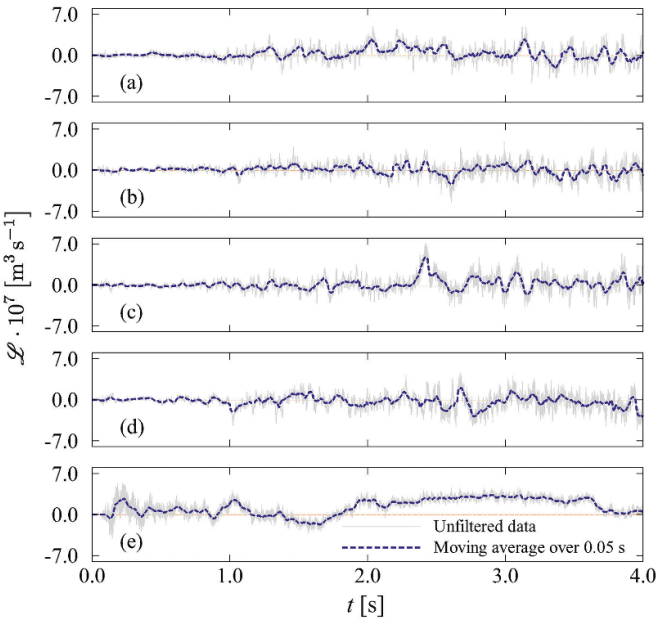

Figure 7. Variations of the averaged angular momentum over the melt-pool surface over a time period of 4 s for (a) Case 1, (b) Case 2, (c) Case 3, (d) Case 4 and (e) Case 5. Unfiltered data: grey lines, Moving average of the data over 0.05 s: dashed blue lines. $\mathscr{L} > 0$ indicates a clockwise rotation.

flow pattern and melt-pool shape, as shown in figure 6. An unsteady, asymmetric, outwardly directed fluid flow emanating from the pool centre is found for all 5 cases. Flow accelerates towards the pool rim, where it meets inwardly directed fluid flow from the rim, due to the change of sign of $(\partial\sigma/\partial T)$ at a certain pool temperature (see figure 2). Close to the region where these two flows meet, velocity magnitudes are high due to the large thermocapillary stresses generated by the steep temperature gradients, in contrast to the low flow velocities in the central region of the pool surface. Interactions between these two opposing flows, and their interactions with the fusion boundary, cause the fluid flow inside the melt pool to be asymmetric and unstable [20], leading to a distorted melt-pool shape.

Melt-pool surface temperatures are roughly 7–16% higher when surface deformations are taken into consideration (Cases 1–4), compared to flat surface simulations (Case 5). Temperature gradients over the melt-pool surface are also on average larger in Cases 1–4 (with a deformable surface) and particularly in Cases 2–4 (with heat source adjustment and/or redistribution), compared to Case 5 (with a non-deformable surface). Consequently, local fluid velocities caused by thermocapillary stresses are almost 25% higher for Cases 1–4, compared to those of Case 5, and are of the order of 0.6 ms^{-1}, in reasonable agreement with experimental measurements performed by Aucott *et al* [8] and estimated values from the scaling analyses also reported by Oreper and Szekely [2], Rivas and Ostrach [57] and Chakraborty and Chakraborty [58].

Free surface deformations have a destabilising effect on the melt pool due to the augmentation of temperature gradients over the melt-pool surface, leading to higher thermocapillary stresses [59]. Additionally, the stagnation region,

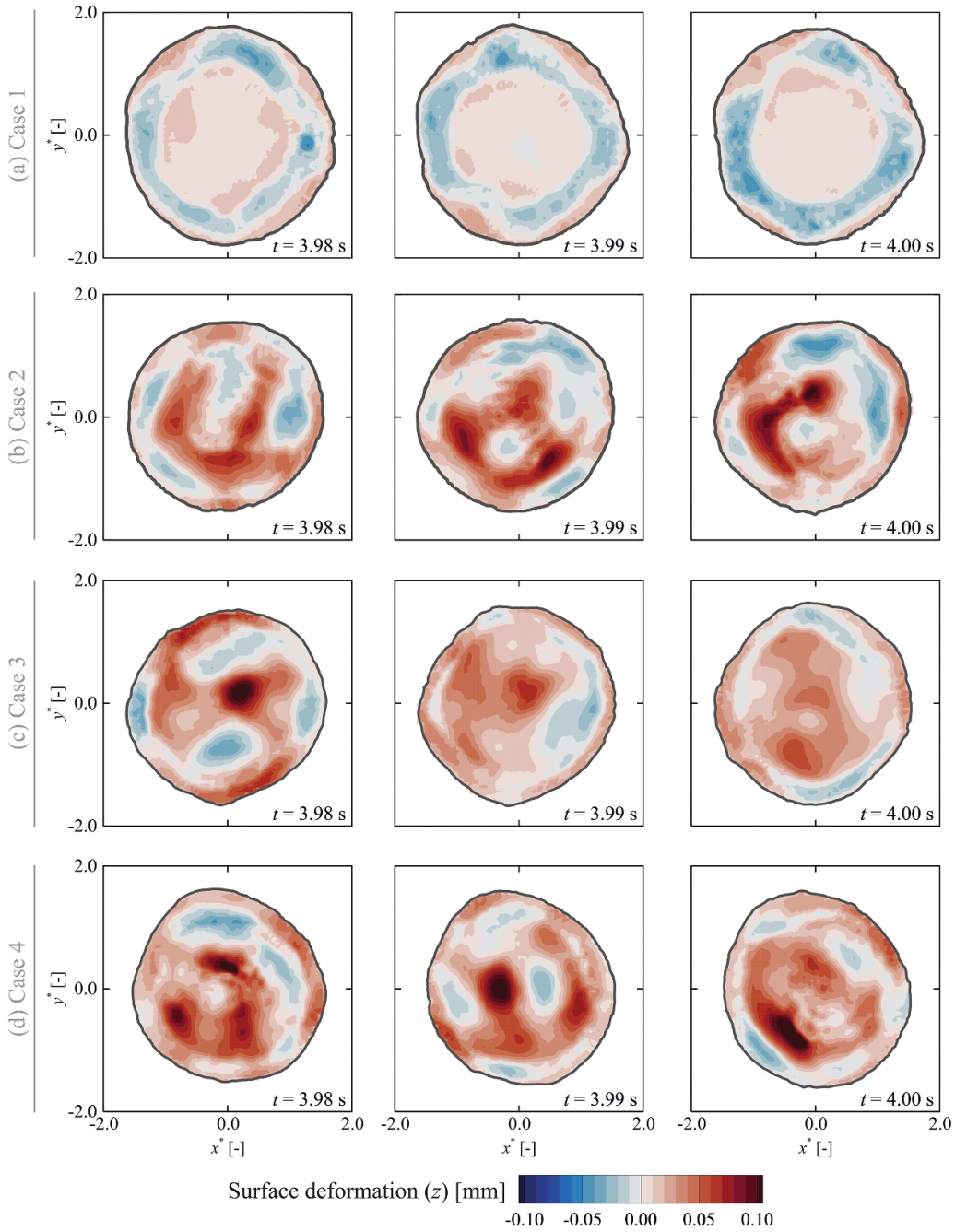

Figure 8. Contours of melt pool free surface deformation at three different time instances for (a) Case 1, (b) Case 2, (c) Case 3, and (d) Case 4. Coordinates are non-dimensionalised using the laser-beam radius r_b as the characteristic length scale. Positive and negative values of z indicate surface depression and elevation, respectively.

where the sign of $(\partial\sigma/\partial T)$ and thus thermocapillary flow direction change, is sensitive to small spatial disturbances and further enhances melt pool instabilities. Furthermore, variations in magnitude and direction of velocities can cause rotational and pulsating fluid motions, leading to cross-cellular flow patterns with a stochastic behaviour in the melt pool [12, 60].

All such flow instabilities reinforce unsteady energy transport from the melt pool to the surrounding solid material, resulting in continuous melting and re-solidification of the material close to the solid-liquid boundary. This complex interplay leads to the melt-pool surface width for Case 5 to be 23% smaller than that for Case 1, and 10% smaller than for Cases 2–4. The higher amount of heat absorbed by the deformed free-surface in Case 1, and the enhanced convective heat transfer in Cases 1–4, are the main causes for the observed pool size differences.

To investigate the rotational fluid motion, the spatially-averaged angular momentum over the melt-pool surface ($\mathscr{L}$) about the z-axis (i.e. the axis of rotation) with respect to the

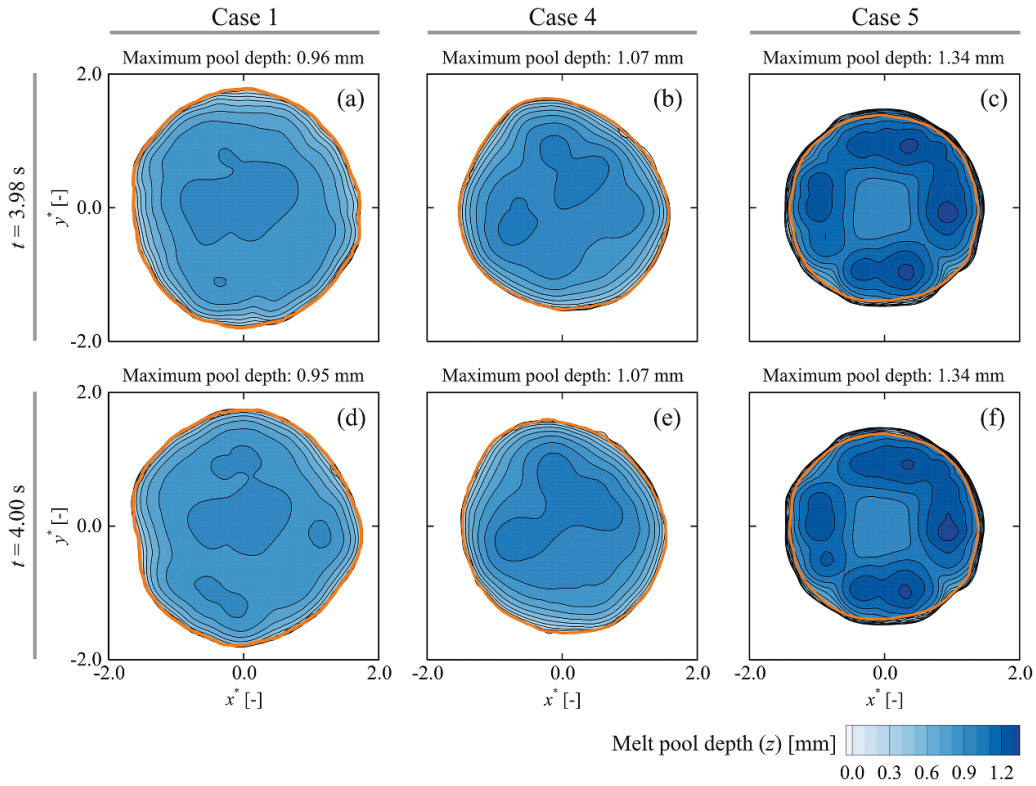

Figure 9. Contours of melt-pool depth at $t = 3.98\,\mathrm{s}$ and $4.00\,\mathrm{s}$ for Cases 1, 4 and 5. Coordinates are non-dimensionalised using the laser-beam radius r_b as the characteristic length scale. The orange circular line shows the melt pool boundary at its top surface.

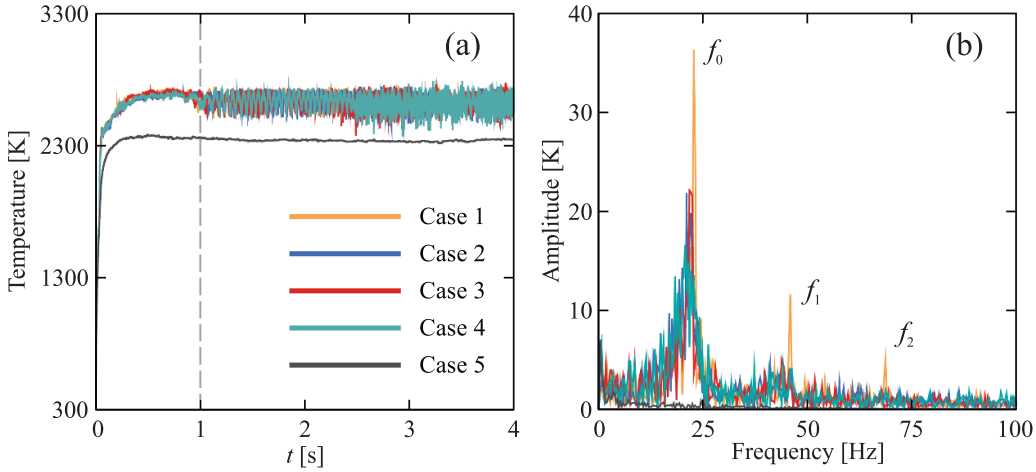

Figure 10. (a) Temperature signals recorded from the monitoring point p_4 located at $(x^*, y^*) = (0, 0)$ on the melt-pool surface and (b) the corresponding frequency spectra. Temperature signals in the period of 1–4 s are employed for FFT analysis.

origin $\mathscr{O}(0,0,0)$ is calculated as follows:

$$\mathscr{L}(t) = \frac{1}{A} \iint_{\text{free surface}} \hat{z} \cdot \left(\vec{r} \times \vec{V}\right) \mathrm{d}A, \tag{24}$$

where $\hat{z}$ is a unit vector in the z-direction, $\vec{r}$ the position vector, $\vec{V}$ velocity vector and A the area of gas-metal interface. Figure 7 shows the temporal variations of angular momentum over the melt-pool surface as a function of time. Positive values of the angular momentum in figure 7 show a clockwise flow rotation, and vice versa. Kidess *et al* [20] applied a similar approach to investigate rotational fluid motion over a flat non-deformable melt-pool surface. Continuous fluctuations in the sign of angular momentum indicate an oscillatory rotational fluid motion in the pool that is indeed self-excited. In Cases 1–4, flow pulsations start to take place after roughly 1 s and continue thereafter. This is not however valid for Case 5, where flow pulsations start to occur already after about 0.1 s, and a clockwise rotation is established after 1.8 s, which lasts for roughly two seconds. These instabilities in the flow field are attributed to a large extent to the interactions between the two opposing flows meeting at the melt-pool surface

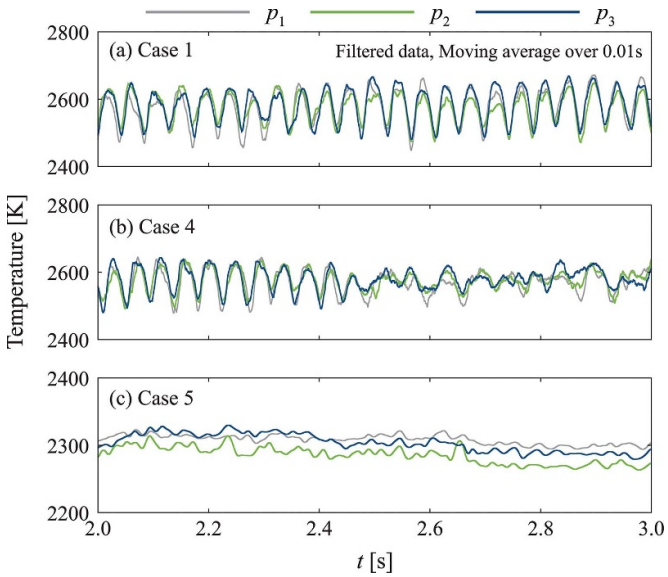

Figure 11. Temperature signals recorded from three monitoring points at the melt pool free surface placed at a radius of 1 mm and along different azimuthal directions ($p_1\,(x^*,y^*) = (5/7,0)$, $p_2\,(x^*,y^*) = (5/7,5/7)$ and $p_3\,(x^*,y^*) = (0,5/7)$). (a) Case 1, (b) Case 4, and (c) Case 5. Signals are smoothed using a moving averaging window of 0.01 s.

[13, 20], and to a lesser extent the effects of hydrothermal waves [61, 62].

Free surface deformations evolve rapidly because of the thermocapillary stresses acting on the melt-pool surface and are shown in figure 8 at three different time instances. Free surface deformations are smaller and less intermittent in Case 1 compared with Cases 2–4. This is due to the smaller thermocapillary stresses and the wider stagnation region, which makes the surface flow field less sensitive to spatial disturbances. Additionally, the Capillary number ($\mathrm{Ca} = \mu\|\vec{V}\|/\sigma$), which represents the ratio between viscous and surface-tension forces and which is $\mathcal{O}(10^{-3})$ for all the cases studied in the present work, appears to be larger in Cases 2–4 ($\mathrm{Ca} \approx 2.5 \times 10^{-3}$) compared with Case 1 ($\mathrm{Ca} \approx 1.5 \times 10^{-3}$), particularly in the central region of the melt-pool surface. Redistributing the energy flux based on the free surface profile (Cases 3 and 4) disturbs the temperature field locally and thus the velocity distribution over the melt-pool surface.

Fluid flow may influence the energy transport and associated phase change significantly during laser melting [7], which can be assessed through the Péclet number that is the ratio between advective and diffusive heat transport, defined as follows:

$$\mathrm{Pe} = \frac{\mathscr{D}\|\vec{V}\|\rho c_\mathrm{p}}{k}, \tag{25}$$

where $\mathscr{D}$ is a characteristic length scale, here chosen to be r_b. The value of the Péclet number is much larger than one ($\mathrm{Pe} = \mathcal{O}(10^2)$), which indicates a large contribution of advection to the total energy transport, compared with diffusion.

The predicted melt-pool depth is shown in figure 9 at two different time instances. When surface deformations are taken into account (Cases 1–4), the predicted melt-pool shape is shallow, with its maximum depth located in the central region and its largest width at the surface. When the surface is assumed to be non-deformable (Case 5), the depth profile of the melt-pool resembles a doughnut-shaped, with its maximum width located below the gas-metal interface. The predicted fusion boundaries of all the cases studied in the present work are asymmetric and unstable. Flow instabilities in the melt pool increase when surface deformations are taken into account, which enhance convection in the pool resulting in a smooth melt-pool depth profile. Variations in the melt-pool shape for Case 5 are less conspicuous compared to those for Cases 1–4 because of the smaller fluctuations in the fluid flow field.

To understand the three-dimensional oscillatory flow behaviour, three monitoring points were selected over the melt-pool surface in different non-azimuthal directions $p_1\,(x^*,y^*) = (5/7,0)$, $p_2\,(x^*,y^*) = (5/7,5/7)$ and $p_3\,(x^*,y^*) = (0,5/7)$ in addition to a point $p_4\,(x^*,y^*) = (0,0)$ on the melt-pool surface, in which x^* and y^* are non-dimensionalized with the laser beam radius r_b. Temperature signals, recorded from the monitoring point p_4, and the corresponding 'fast Fourier transform' (FFT) [63] frequency spectra are shown in figure 10. In the presence of surface deformations (Cases 1–4), self-excited temperature fluctuations, initiated by numerical noise, grow and reach a quasi-steady state after about 1 s. Without surface deformations (Case 5), the amplitudes of temperature fluctuations remain very small. In Case 1, where surface deformations are taken into account, the temperature fluctuations with large amplitudes have a fundamental frequency of $f_0 \approx 22$ Hz, with harmonics at $f_1 \approx 2f_0$ and $f_2 \approx 3f_0$. Irregular patterns appear in the spectrum of temperature fluctuations for Case 2–4, showing a highly unsteady behaviour that results from the enhancement of thermocapillary stresses and the variations in energy flux distribution.

Temperature signals recorded from monitoring points p_1, p_2 and p_3 in the time interval of 2–3 s are shown in figure 11. The data for Case 1 indicate that the thermal and fluid flow fields are dominated by a pulsating behaviour. This is also valid for Case 4 up to roughly 2.5 s; however, after 2.5 s modulation of temperature fluctuations takes place, which is probably due to changes in temperature gradients, melt pool size and the complex interactions between vortices generated inside the melt pool. Similar behaviour was observed for Cases 2 and 3 (not shown here). The amplitudes of temperature fluctuations appear to be smaller for Case 5 compared to the other cases and show an irregular behaviour, revealing complex unsteady flow in the melt pool.

4.3. The effects of employing temperature-dependent material properties

In this section, the effects of employing temperature-dependent properties on numerical predictions of thermal and flow fields as well as the melt-pool shape are investigated using two different heat source models (Cases 1 and 4). Temperature-dependent properties for the metallic alloy

Table 4. Temperature-dependent thermophysical properties of the Fe–S alloy used in the present study. Values are estimated by analogy with the values for iron-based alloys [64].

Property	Fe-S alloy	Unit
Density ρ	8100	kg m^{-3}
Specific heat capacity c_p	627 (solid phase) 723.14 (liquid phase)	J kg^{-1} K^{-1}
Thermal conductivity k	8.8521+0.0114·T (solid phase) 4.5102+0.0107·T (liquid phase)	W m^{-1} K^{-1}
Viscosity μ	$0.0659 - 7 \times 10^{-5} \cdot T + 3 \times 10^{-8} \cdot T^2 - 3 \times 10^{-12} \cdot T^3$	kg m^{-1} s^{-1}
Latent heat of fusion L_f	250 800	J kg^{-1}
Thermal expansion coefficient β	2×10^{-6}	K^{-1}
Liquidus temperature T_l	1620	K
Solidus temperature T_s	1610	K

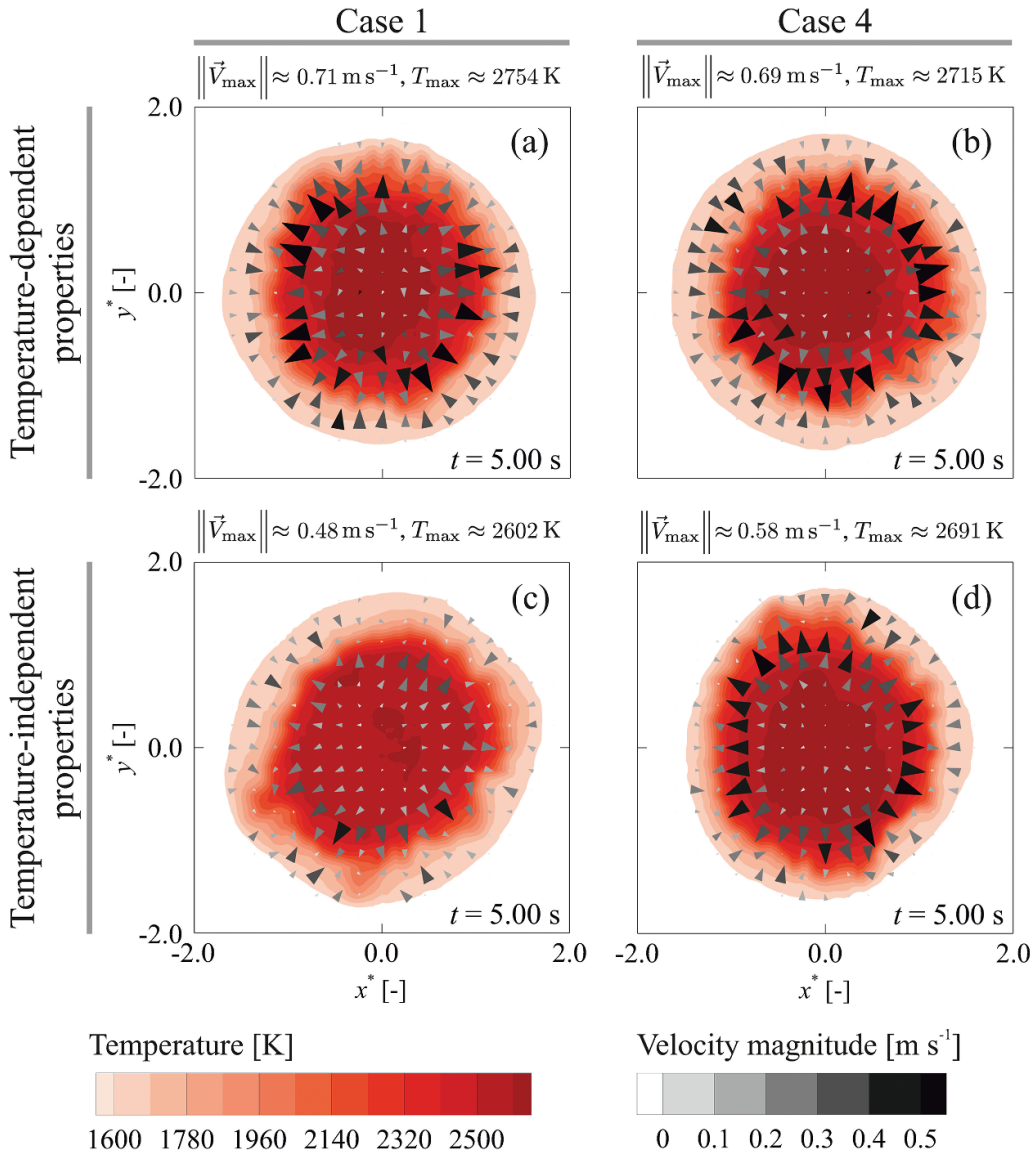

Figure 12. Contours of temperature and the velocity vectors on the melt pool free surface after 5 s of heating predicted using the heat source models Cases 1 and 4 with temperature-dependent (table 4) and temperature-independent (table 1) material properties. Coordinates are non-dimensionalised using the laser-beam radius r_b as the characteristic length scale.

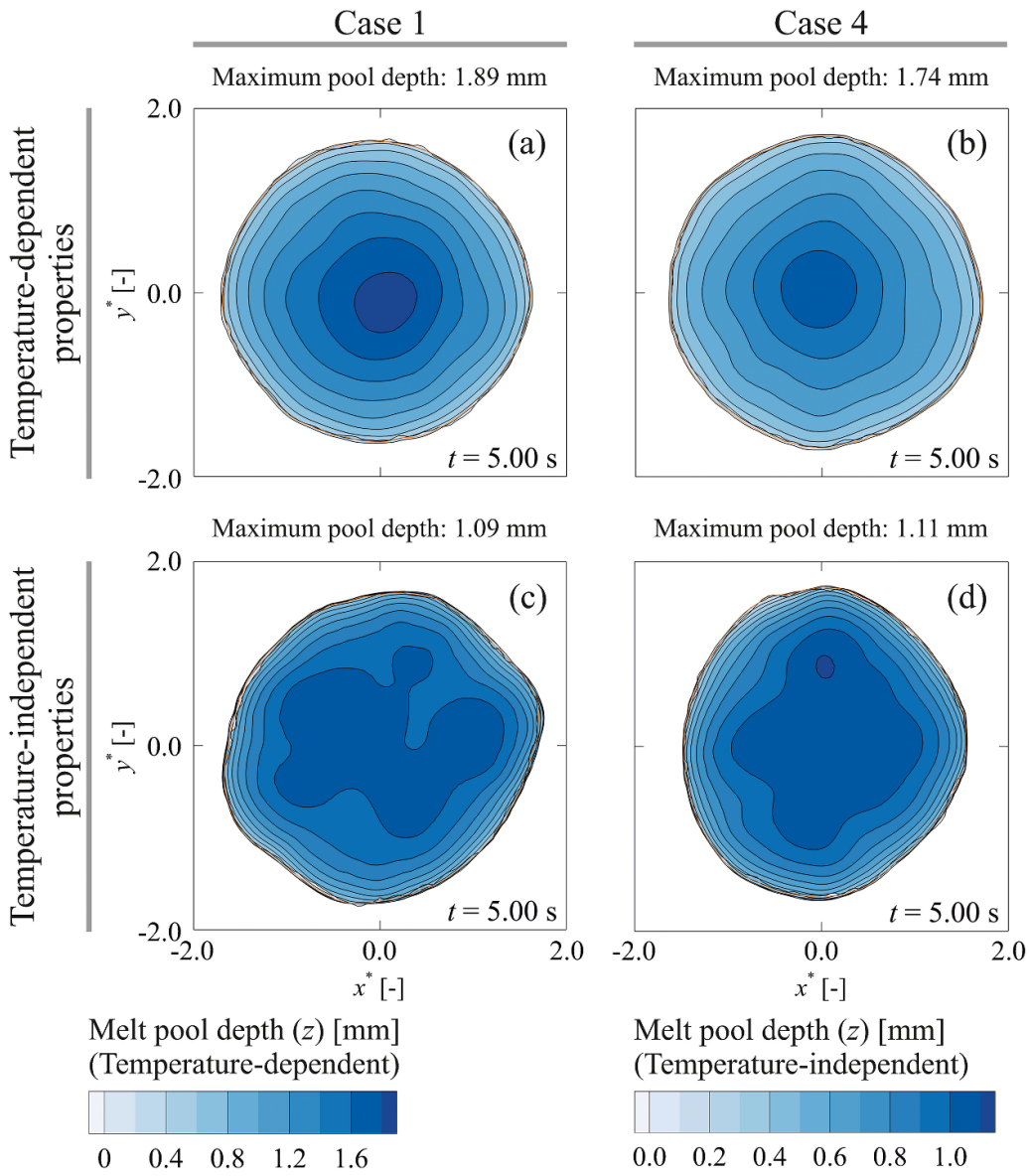

Figure 13. Contours of melt-pool depth at 5 s for Cases 1 and 4 predicted using temperature-dependent and temperature-independent material properties. Coordinates are non-dimensionalised using the laser-beam radius r_b as the characteristic length scale. The orange circular line shows the melt pool boundary at its top surface.

considered in the present study (S705) are given in table 4, where the values are estimated by analogy with the values for iron-based alloys [64]. Temperature distribution over the melt-pool surface and free-surface flow after 5 s of heating are shown in figure 12 for both temperature-dependent and temperature-independent thermophysical properties. Melt-pool surface temperatures predicted using temperature-independent properties are about 1–6% lower than those predicted using temperature-dependent properties. This is mainly attributed to the changes in the thermal diffusivity $(\alpha = k/(\rho c_p))$ of the molten material. The thermal conductivity of the molten material changes from $21.8\,\mathrm{W\,m^{-1}\,K^{-1}}$ at $T = 1620\,\mathrm{K}$ to $33.4\,\mathrm{W\,m^{-1}\,K^{-1}}$ at $T = 2700\,\mathrm{K}$. Hence, the average thermal diffusivity of the molten material obtained from a temperature-dependent model is about 10% lower than that estimated using temperature-independent properties. The fluid velocities are roughly 15–32% lower when temperature-independent properties are employed, compared to those predicted using temperature-dependent properties, which is due to the decrease in the viscosity of the molten material at elevated temperatures. With an increase in temperature, the thermal conductivity of the molten metal increases and the viscosity of the molten metal decreases, resulting in a reduction of momentum diffusivity and enhancement of thermal diffusivity and thus reduction of the Prandtl number $(\mathrm{Pr} = c_p\,\mu/k)$. Although the heat source models affect the thermal and flow fields in the melt pool, it is found that the numerical predictions are less sensitive to the heat source models when temperature-dependent properties are employed for the cases studied in the present work. However, it should be noted that for the cases where surface deformations are larger, the effects of heat source adjustment

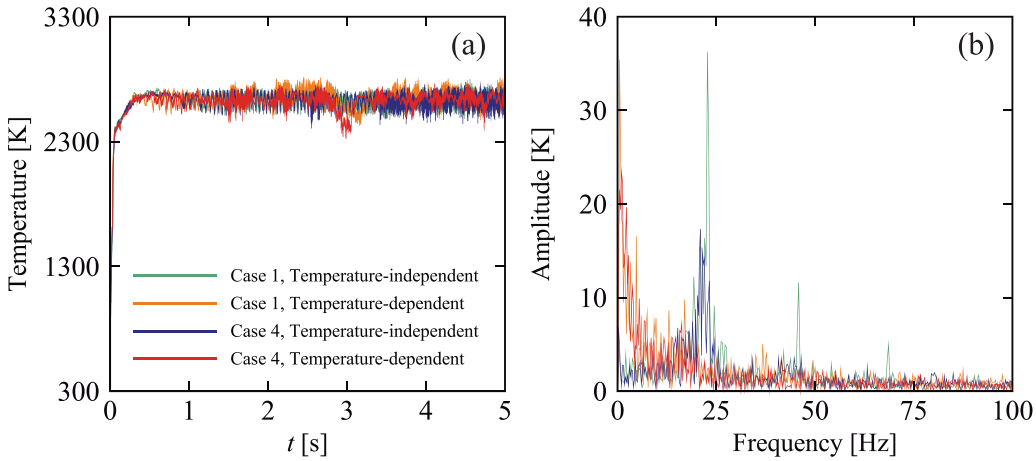

Figure 14. The influence of employing temperature-dependent material properties on temperature signals received from the melt pool and the corresponding frequency spectra. (a) Temperature signals recorded from the monitoring point p_4 located at $(x^*, y^*) = (0, 0)$ on the melt-pool surface and (b) the corresponding frequency spectra. Temperature signals in the period of 1–5 s are employed for FFT analysis.

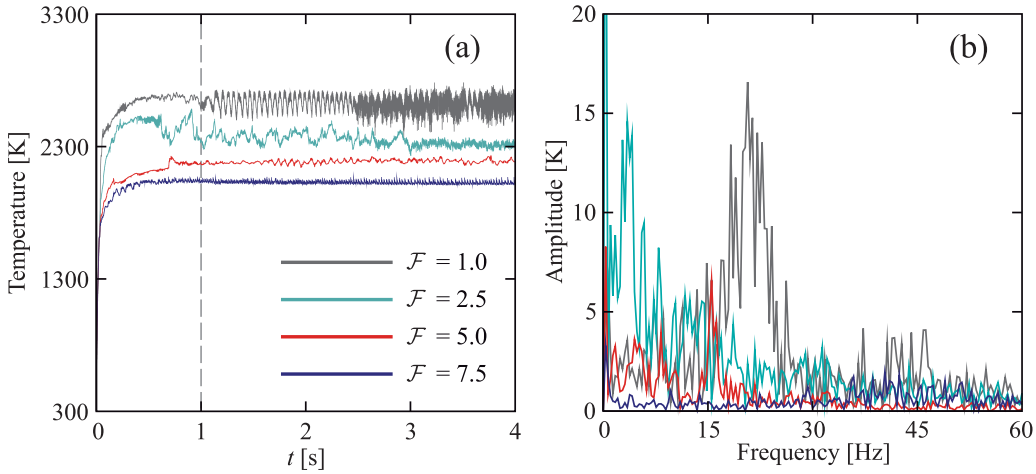

Figure 15. (a) Temperature signals recorded from the monitoring point p_4 $(x^*, y^*) = (0, 0)$ on the melt-pool surface and (b) the corresponding frequency spectra for different values of the enhancement factor $\mathcal{F}$. Temperature signals in the period of 1–4 s are employed for FFT analysis.

on numerical predictions become critical, as discussed in section 4.2.

Changes in the material properties with temperature affect thermal and flow fields in the melt pool, resulting in changes in the predicted melt-pool shape, as shown in figure 13. When temperature-dependent properties are employed, the melt-pool depth is significantly (about 36–74%) larger than that predicted using temperature-independent properties.

Temperature signals recorded from the monitoring point p_4 and the corresponding frequency spectra are shown in figure 14. Temperature signals received from the monitoring point p_4 are almost in the same range and vary between 2320 K and 2820 K. Employing temperature-dependent properties affects the frequency spectra of fluctuations, however the amplitude of fluctuations remains almost unaffected. The results presented in figure 14 indicate that adjusting the heat source dynamically during simulations can result in a decrease in the amplitude of temperature fluctuations, however its effect on the frequency spectrum is insignificant.

4.4. The effects of the enhancement factor

In section 4.1 it was mentioned that, in many simulation studies in literature, the thermal conductivity and viscosity of the liquid metal were artificially increased by a so-called enhancement factor $\mathcal{F}$, in order to obtain better agreement between experimental and simulated post-solidification melt-pool shapes. Numerical studies carried out by De *et al* [65–67] showed that the values reported for the enhancement factor in the literature depend greatly on operating conditions and ranges from 2 to 100 (see for instance, [68–71]), however values between 2 and 10 are most often employed. The effects of the enhancement factor $\mathcal{F}$ on thermal and fluid flow fields in molten metal melt pools as well as the melt-pool shape can be found in [19, 43, 45], thus are not repeated here. Focusing on Case 4 in which free surface deformations are accounted for, the influence of $\mathcal{F}$ on the oscillatory flow behaviour is investigated. Temperatures recorded from the monitoring point p_4 and the temperature fluctuation spectra are shown in figure 15.

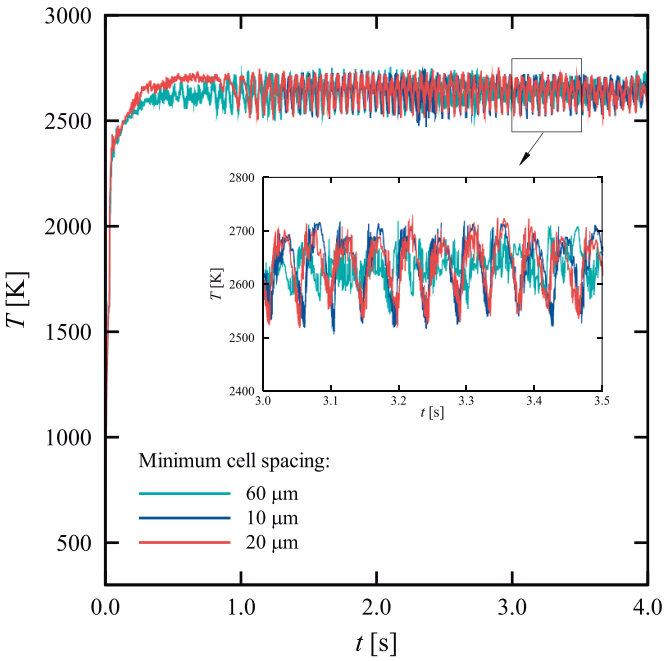

Figure 16. Temperature variations predicted at the melt pool centre using different grid sizes. The grid with minimum cell spacing of 20 μm was employed for the calculations reported in the paper.

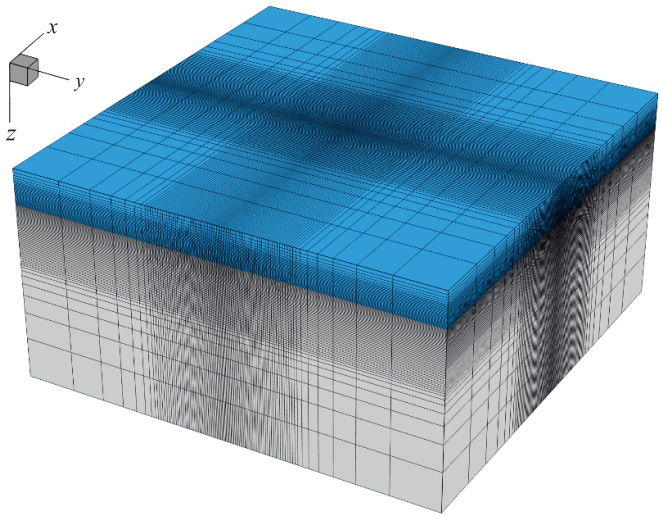

Figure 17. The computational grid employed for the present calculations reported in the paper. Regions highlighted in blue show the gas layer above the base material.

Temperatures and the amplitudes of fluctuations reduce with increasing $\mathcal{F}$. The contribution of diffusion in total energy transport increases with $\mathcal{F}$, which results in a reduction of temperature gradients and therefore thermocapillary stresses generated over the melt-pool surface. The reduced thermocapillary stresses in addition to the enhanced viscosity of the molten metal lead to a reduction of fluid velocities that decrease convection in the melt pool further, which significantly affects the fluid flow structure. Increasing $\mathcal{F}$ to 2.5 results in relatively deeper melt pool with a corresponding reduction of the fundamental frequency of fluctuations. Using higher values of $\mathcal{F}$, the melt-pool shape approaches a spherical-cap shape and the frequency spectrum becomes rather uniform with small amplitude fluctuations.

5. Conclusions

Molten metal melt pool behaviour during a laser spot melting process was studied to investigate the influence of dynamically adjusted energy flux distribution on thermal and fluid flow fields using both deformable and non-deformable gas–metal interfaces.

For the material and laser power studied in the present work, self-excited flow instabilities arise rapidly and fluid flow inside the melt pool is inherently three-dimensional and unstable. Flow instabilities in the melt pool have a significant influence on solidification and melting by altering the thermal and fluid flow fields. Free surface deformations, even small compared to the melt pool size, can significantly influence the fluid flow pattern in the melt pool. When in the numerical simulations the gas-metal interface is assumed to remain flat and non-deformable, lower temperatures with smaller fluctuations were found in comparison to those of the cases with a deformable interface, which results in a different melt-pool shape. Taking the surface deformations into account leads to erratic flow patterns with relatively large fluctuations, which are caused by the intensified interactions between vortices generated in the melt pool resulting from the augmented thermocapillary stresses. When surface deformations are taken into account, various tested methods for adjusting the absorbed energy flux resulted in smaller melt-pool sizes compared to those without an adjustment. However, the melt pool behaves quite similarly for various adjustment methods studied in the present work. This should be noted that the utilisation of temperature-dependent properties can enhance the accuracy of numerical predictions in simulations of molten metal flow in melting pools; however, the results presented in the present work show the importance of employing a physically-realistic heat-source model that is also applicable if temperature-dependent properties were employed.

Although the enhancement factors are widely used to achieve agreement between numerically predicted melt-pool sizes and solidification rates with experiments, they do not represent the physics of complex transport phenomena governing laser spot melting. The use of an enhancement factor can significantly affect the numerical predictions of melt pool oscillatory behaviour.

Author contributions

Conceptualisation, A E, C R K and I M R; methodology, A E; software, A E; validation, A E; formal analysis, A E; investigation, A E; resources, A E, C R K, and I M R; data curation, A E; writing—original draft preparation, A E; writing—review

Table A1. The influence of computational cell size on predicted melt pool size.

Minimum cell spacing	Total number of cells	Melt pool width	Melt pool depth
60 μm	5.5×10^5	4.89 mm	1.09 mm
20 μm	8.6×10^5	4.88 mm	0.96 mm
10 μm	2.1×10^6	4.88 mm	0.95 mm

and editing, A E, C R K, and I M R; visualisation, A E; supervision, C R K and I M R; project administration, A E and I M R; and funding acquisition, I M R.

Conflict of interest

The authors declare no conflict of interest.

Acknowledgments

This research was carried out under project number F31.7.13504 in the framework of the Partnership Program of the Materials innovation institute M2i (www.m2i.nl) and the Foundation for Fundamental Research on Matter (FOM) (www.fom.nl), which is part of the Netherlands Organisation for Scientific Research (www.nwo.nl). The authors would like to thank the industrial partner in this project "Allseas Engineering B V" for the financial support.

Appendix A. Grid independence test

Case 1 was considered for grid independence test. Three different grids with minimum cell spacings of 60, 20 and 10 μm were studied. The influence of computational cell size on predicted melt pool depth and width are reported in table A1, which indicate the predictions are reasonably independent of the grid size. The variations of temperature at the centre of the melt pool surface (*i.e.,* $T(0, 0, z_{\text{surface}})$) were also investigated for different grid sizes and the results are shown in figure 16. The grid with minimum cell size of 20 μm was employed for the present calculations reported in the paper, and is shown in figure 17.

ORCID iDs

Amin Ebrahimi https://orcid.org/0000-0002-4912-2549
Chris R Kleijn https://orcid.org/0000-0001-6821-0969
Ian M Richardson https://orcid.org/0000-0002-3651-3233

References

[1] Ayoola W, Suder W and Williams S 2017 Parameters controlling weld bead profile in conduction laser welding *J. Mater. Process. Technol.* **249** 522–30
[2] Oreper G M and Szekely J 1984 Heat- and fluid-flow phenomena in weld pools *J. Fluid Mech.* **147** 53
[3] Mills K C, Keene B J, Brooks R F and Shirali A 1998 Marangoni effects in welding *Phil. Trans. R. Soc.* A **356** 911–25
[4] Heiple C R and Roper J R 1982 Mechanism for minor element effect on GTA fusion zone geometry *Weld J.* **61** 97s–102s
[5] Paul A and DebRoy T 1988 Free surface flow and heat transfer in conduction mode laser welding *Metall. Trans.* B **19** 851–8
[6] Cook P S and Murphy A B 2020 Simulation of melt pool behaviour during additive manufacturing: Underlying physics and progress *Additive Manuf.* **31** 100909
[7] DebRoy T and David S A 1995 Physical processes in fusion welding *Rev. Mod. Phys.* **67** 85–112
[8] Aucott L *et al* 2018 Revealing internal flow behaviour in arc welding and additive manufacturing of metals *Nat. Commun.* **9** 5414
[9] Zacharia T, David S A, Vitek J M and Debroy T 1990 Modeling of interfacial phenomena in welding *Metall. Trans.* B **21** 600–3
[10] Ha E-J and Kim W-S 2005 A study of low-power density laser welding process with evolution of free surface *Int. J. Heat Fluid Flow* **26** 613–21
[11] Shah A, Kumar A and Ramkumar J 2018 Analysis of transient thermo-fluidic behavior of melt pool during spot laser welding of 304 stainless-steel *J. Mater. Process. Technol.* **256** 109–20
[12] Zhao C, Kwakernaak C, Pan Y, Richardson I, Saldi Z, Kenjeres S and Kleijn C 2010 The effect of oxygen on transitional marangoni flow in laser spot welding *Acta Mater.* **58** 6345–57
[13] Kidess A, Kenjereš S, Righolt B W and Kleijn C R 2016 Marangoni driven turbulence in high energy surface melting processes *Int. J. Thermal Sci.* **104** 412–22
[14] Hirt C and Nichols B 1981 Volume of fluid (VOF) method for the dynamics of free boundaries *J. Comput. Phys.* **39** 201–25
[15] Meng X, Qin G and Zou Z 2016 Investigation of humping defect in high speed gas tungsten arc welding by numerical modelling *Mater. Des.* **94** 69–78
[16] Wu D, Nguyen A V, Tashiro S, Hua X and Tanaka M 2019 Elucidation of the weld pool convection and keyhole formation mechanism in the keyhole plasma arc welding *Int. J. Heat Mass Transfer* **131** 920–31
[17] Choo R T C, Szekely J and Westhoff R C 1990 Modeling of high-current arcs with emphasis on free surface phenomena in the weld pool *Weld J.* **69** 346–61
[18] Pitscheneder W, DebRoy T, Mundra K and Ebner R 1996 Role of sulfur and processing variables on the temporal evolution of weld pool geometry during multikilowatt laser beam welding of steels *Weld J.* **75** 71–80
[19] Saldi Z, Kidess A, Kenjereš S, Zhao C, Richardson I and Kleijn C 2013 Effect of enhanced heat and mass transport and flow reversal during cool down on weld pool shapes in laser spot welding of steel *Int. J. Heat Mass Transfer* **66** 879–88
[20] Kidess A, Kenjereš S and Kleijn C R 2016 The influence of surfactants on thermocapillary flow instabilities in low prandtl melting pools *Phys. Fluids* **28** 062106

[21] Heiple C R, Roper J R, Stagner R T and Aden R J 1983 Surface active element effects on the shape of GTA, laser and electron beam welds *Weld J.* **62** 72s–77s

[22] Mills K C and Keene B J 1990 Factors affecting variable weld penetration *Int. Mater. Rev.* **35** 185–216

[23] Sahoo P, Debroy T and McNallan M J 1988 Surface tension of binary metal—surface active solute systems under conditions relevant to welding metallurgy *Metall. Trans.* B **19** 483–91

[24] Zacharia T, Eraslan A H, Aidun D K and David S A 1989 Three-dimensional transient model for arc welding process *Metall. Trans.* B **20** 645–59

[25] Cho J, Farson D F, Hollis K J and Milewski J O 2015 Numerical analysis of weld pool oscillation in laser welding *J. Mech. Sci. Technol.* **29** 1715–22

[26] Kim Y-D and Kim W-S 2008 A numerical analysis of heat and fluid flow with a deformable curved free surface in a laser melting process *Int. J. Heat Fluid Flow* **29** 1481–93

[27] Voller V R and Swaminathan C R 1991 General source-based method for solidification phase change *Numer. Heat Transfer* B **19** 175–89

[28] Voller V and Prakash C 1987 A fixed grid numerical modelling methodology for convection-diffusion mushy region phase-change problems *Int. J. Heat Mass Transfer* **30** 1709–19

[29] Ebrahimi A, Kleijn C R and Richardson I M 2019 Sensitivity of numerical predictions to the permeability coefficient in simulations of melting and solidification using the enthalpy-porosity method *Energies* **12** 4360

[30] Sun Y and Beckermann C 2004 Diffuse interface modeling of two-phase flows based on averaging: mass and momentum equations *Phys.* D **198** 281–308

[31] Brackbill J, Kothe D and Zemach C A 1992 continuum method for modeling surface tension *J. Comput. Phys.* **100** 335–54

[32] Belton G R 1976 Langmuir adsorption, the Gibbs adsorption isotherm and interracial kinetics in liquid metal systems *Metall. Trans.* B **7** 35–42

[33] March N H and Tosi M P 1991 *Atomic Dynamics in Liquids* (New York: Dover)

[34] Gao X, Wu C, Goecke S and Kügler H 2017 Numerical simulation of temperature field, fluid flow and weld bead formation in oscillating single mode laser-GMA hybrid welding *J. Mater. Process. Technol.* **242** 147–59

[35] Ebrahimi A, Kleijn C R and Richardson I M 2021 A simulation-based approach to characterise melt-pool oscillations during gas tungsten arc welding *Int. J. Heat Mass Transfer* **164** 120535

[36] Arrizubieta J I, Lamikiz A, Klocke F, Martínez S, Arntz K and Ukar E 2017 Evaluation of the relevance of melt pool dynamics in laser material deposition process modeling *Int. J. Heat Mass Transfer* **115** 80–91

[37] Amara E H and Fabbro R 2010 Modeling of humps formation during deep-penetration laser welding *App. Phys. A* **101** 111–16

[38] Indhu R, Vivek V, Sarathkumar L, Bharatish A and Soundarapandian S 2018 Overview of laser absorptivity measurement techniques for material processing *Lasers Manuf. Mater. Process.* **5** 458–81

[39] ANSYS® Fluent *Release 18.1*

[40] Patankar S V 1980 *Numerical Heat Transfer and Fluid Flow*, 1st edn (London: Taylor & Francis Inc)

[41] Issa R 1986 Solution of the implicitly discretised fluid flow equations by operator-splitting *J. Comput. Phys.* **62** 40–65

[42] Ubbink O 1997 Numerical prediction of two fluid systems with sharp interfaces *Doctoral Thesis* Imperial College London University of London London, United Kingdom (http://hdl.handle.net/10044/1/8604)

[43] Ehlen G, Ludwig A and Sahm P R 2003 Simulation of time-dependent pool shape during laser spot welding: Transient effects *Metall. Mater. Trans.* A **34** 2947–61

[44] Ebrahimi A, Kleijn C R and Richardson I M 2019 The influence of surface deformation on thermocapillary flow instabilities in low Prandtl melting pools with surfactants *Proc. 5th World Congress on Mechanical, Chemical and Material Engineering* (Avestia Publishing) (https://doi.org/10.11159/htff19.201)

[45] Mundra K, DebRoy T, Zacharia T and David S A 1992 Role of thermophysical properties in weld pool modeling *Weld J.* **71** 313–20

[46] Do-Quang M, Amberg G and Pettersson C-O 2008 Modeling of the adsorption kinetics and the convection of surfactants in a weld pool *J. Heat Transfer* **130** 092102

[47] Winkle C, Amberg G, Inoue H, Koseki T and Fuji M 2000 Effect of surfactant redistribution on weld pool shape during gas tungsten arc welding *Sci. Technol. Weld. Join.* **5** 8–20

[48] Tsai M C and Kou S 1989 Marangoni convection in weld pools with a free surface *Int. J. Numer. Methods Fluids* **9** 1503–16

[49] He X, Fuerschbach P W and DebRoy T 2003 Heat transfer and fluid flow during laser spot welding of 304 stainless steel *J. Phys. D: Appl. Phys.* **36** 1388–98

[50] Cunningham R, Zhao C, Parab N, Kantzos C, Pauza J, Fezzaa K, Sun T and Rollett A D 2019 Keyhole threshold and morphology in laser melting revealed by ultrahigh-speed x-ray imaging *Science* **363** 849–52

[51] Sharma S, Mandal V, Ramakrishna S and Ramkumar J 2018 Numerical simulation of melt hydrodynamics induced hole blockage in quasi-CW fiber laser micro-drilling of TiAl6V4 *J. Mater. Process. Technol.* **262** 131–48

[52] Lee J Y, Ko S H, Farson D F and Yoo C D 2002 Mechanism of keyhole formation and stability in stationary laser welding *J. Phys. D: Appl. Phys.* **35** 1570–6

[53] von Allmen M and Blatter A 1995 *Laser-Beam Interactions With Materials* (Berlin: Springer)

[54] Mukherjee S, Zarghami A, Haringa C, van As K, Kenjereš S and den Akker H E V 2018 Simulating liquid droplets: A quantitative assessment of lattice Boltzmann and volume of fluid methods *Int. J. Heat Fluid Flow* **70** 59–78

[55] Courtois M, Carin M, Masson P L, Gaied S and Balabane M 2016 Guidelines in the experimental validation of a 3D heat and fluid flow model of keyhole laser welding *J. Phys. D: Appl. Phys.* **49** 155503

[56] Bergström D, Powell J and Kaplan A F H 2007 A ray-tracing analysis of the absorption of light by smooth and rough metal surfaces *J. Appl. Phys.* **101** 113504

[57] Rivas D and Ostrach S 1992 Scaling of low-Prandtl-number thermocapillary flows *Int. J. Heat Mass Transfer* **35** 1469–79

[58] Chakraborty N and Chakraborty S 2007 Thermal transport regimes and generalized regime diagram for high energy surface melting processes *Metall. Mater. Trans.* B **38** 143–7

[59] Davis S H and Homsy G M 1980 Energy stability theory for free-surface problems: buoyancy-thermocapillary layers *J. Fluid Mech.* **98** 527

[60] Czerner S 2005 Schmelzbaddynamik beim Laserstrahl-Wärmeleitungsschweiβen von Eisenwerkstoffen *PhD Thesis* Leibniz Universität Hannover (http://nbn-resolving.de/urn: nbn:de:gbv:089-4942690490)

[61] Kuhlmann H C and Schoisswohl U 2010 Flow instabilities in thermocapillary-buoyant liquid pools *J. Fluid Mech.* **644** 509

[62] Davis S H 1987 Thermocapillary instabilities *Annu. Rev. Fluid Mech.* **19** 403–35

[63] Temperton C 1985 Implementation of a self-sorting in-place prime factor FFT algorithm *J. Comput. Phys.* **58** 283–99
[64] Mills K C 2002 *Recommended Values of Thermophysical Properties for Selected Commercial Alloys* (Cambridge: Woodhead)
[65] De A and DebRoy T 2006 Improving reliability of heat and fluid flow calculation during conduction mode laser spot welding by multivariable optimisation *Sci. Technol. Weld. Join.* **11** 143–53
[66] De A and DebRoy T 2005 Reliable calculations of heat and fluid flow during conduction mode laser welding through optimization of uncertain parameters *Weld J.* **84** 101–12
[67] De A and DebRoy T 2004 A smart model to estimate effective thermal conductivity and viscosity in the weld pool *J. Appl. Phys.* **95** 5230–40
[68] Zhang W, Roy G G, Elmer J W and DebRoy T 2003 Modeling of heat transfer and fluid flow during gas tungsten arc spot welding of low carbon steel *J. Appl. Phys.* **93** 3022–33
[69] Choo R T C and Szekely J 1994 Possible role of turbulence in GTA weld pool behavior *Weld J.* **73** 25–31
[70] Mundra K and DebRoy T 1993 Toward understanding alloying element vaporization during laser beam welding of stainless steel *Weld J.* **72** 1–9
[71] Choo R T C, Szekely J and Westhoff R C 1992 On the calculation of the free surface temperature of gas-tungsten-arc weld pools from first principles: part I. modeling the welding arc *Metall. Mater. Trans.* B **23** 357–69